ARTICLE

Mesoscale Structure of Trade Wind Convection over Puerto Rico: Composite Observations and Numerical Simulation

Mark R. Jury · Sen Chiao · Eric W. Harmsen

Abstract We examine the mesoscale structure of the atmospheric boundary layer (ABL), low-level circulation, and trade wind convection over the sub-tropical island of Puerto Rico in mid-summer. Shallow afternoon thunderstorms are frequently seen over the western plains of the island. Observational data include automatic weather station measurements, radiosonde profiles, infrared satellite images, and mesoscale reanalysis data with a focus on the summer of 2006. Satellite microwave radar data (TRMM and CloudSat) indicate that island clouds typically extend just above the $-20°C$ level during afternoon hours with reflectivity values reaching 50 dBz. A singular value decomposition of 3-hourly high resolution satellite rainfall maps reveals an island mode. From this a composite is constructed for a group of ten cases. With a Froude number ≈ 1 the trade winds pass over the mountains and standing vortices and gravity waves are trapped in the meandering wake. The Weather and Research Forecasting (WRF) model at 1-km resolution with 51 vertical layers is used to simulate the short-lived thunderstorms for two cases: 27 June and 20 July 2006. The model correctly locates the convective cells that develop between 1400 and 1700 LST. The shallow afternoon thunderstorms are triggered by surface heat fluxes, confluent sea breezes and a mountain wake. Recommendations for enhanced observations are given.

Keywords Caribbean island · Sea-breeze confluence · Trade wind convection

M. R. Jury (✉)
Physics Department, University of Puerto Rico, Mayaguez, PR 00681, USA
e-mail: jury@uprm.edu

S. Chiao
Florida Institute of Technology, Melbourne, FL 32901, USA

E. W. Harmsen
Agricultural Engineering Department, UPRM, Mayaguez, USA

⚄ Springer

1 Introduction

The importance of atmospheric boundary-layer (ABL) convergence zones that initiate vertical motion and moist convection has long been recognized (Malkus 1955). Frictional drag and surface heat fluxes affect local weather through their bottom-up imprint on the ABL. Convective clouds are often located along lines of topographic and thermally generated wind shear (Wilson and Schreiber 1986), more commonly known as mountain wakes and sea breezes. Over the Florida peninsula, land-sea breeze circulations are often seen to generate convergence and afternoon thunderstorms (Cooper et al. 1982; Blanchard and López 1985; Wakimoto and Atkins 1994; Kingsmill 1995). An understanding of these processes can aid short-range local weather forecasts.

The ABL over west Pacific tropical islands has been analyzed by Keenan et al. (2000) during summer when thunderstorms are prevalent. The convection was related to a confluent coastal circulation driven by daytime heating (Liu and Moncrieff 1996), with large-scale easterly flow opposed by low-level westerly seabreezes (Carbone et al. 2000). Cloud tops penetrated above 15 km by mid-afternoon and decayed by sunset. The convective wake that extends downstream from sub-tropical islands has been studied by Smith et al. (1997), who distinguished between a long, steady, narrow mountain wake when the trade wind inversion is present, and a wider turbulent wake in unstable conditions (Schar and Smith 1993a,b; Grubisic et al. 1995). The flow can accelerate over and around islands, then undergo hydraulic deceleration. The island's frictional drag may interact with the downstream wake to produce a pair of counter-rotating eddies and associated vorticity dipole. Depending on the Reynolds number and mountain height, either standing waves or drifting eddies can be shed. Wakes and quasi-stationary eddies near mountainous islands have been seen in satellite cloud patterns (Chopra 1973; Etling 1989). Extensive aerial surveys have been conducted around the Hawaiian Islands (Smith and Grubisic 1993), and the structure of the trade wind flow has been simulated using mesoscale models (Burk et al. 2002).

Puerto Rico is an island in the central Caribbean of dimension 70×200 km, with a zonal oriented mountain ridge that reaches 1,000 m elevation (Fig. 1a). It is densely vegetated (Fig. 1b) and endowed with water resources to support a population that is one of the densest in the world. Puerto Rico is bordered by the warm Caribbean Sea on its southern flank (18.1–18.4°N, 67.5–65.5°W), and the surrounding sea-surface temperatures (SST) exceed 28°C during summer (Fig. 1c) so the air mass is thermodynamically driven and convective. Trade winds prevail over 80% of the time at this latitude and there are only a few small islands upwind to the east. The island is of sufficient area and height to generate its own circulation, wakes and ABL structure. Convective clouds tend to form over the leeward interior and western coastal plains following midday heating. Aircraft measurements have been collected around Puerto Rico during trade wind conditions (Malkus 1955) and a symmetric orographic-convection cell with ascent over the island and compensating subsidence in a surrounding ring was found. A moisture budget was proposed for the aircraft cross-section, and the effects of vertical motions and ABL heating imposed on the air stream in its passage over the island were outlined in the context of water vapour transport, cloud structure and seabreeze development (Pearce et al. 1956). The mesoscale circulation plays a significant role in the formation of afternoon thunderstorms. In a two-layer model simulation with steady easterly flow (Bennet et al. 1998), a trapped lee-side wave formed west of the central mountains in response to mid-day heating. North-easterly (south-easterly) trade winds accelerated along the north (south) coast, and reversed over the west coast at the time of maximum solar influx. The resulting confluence induced uplift and cloud formation over the western interior consistent with observations.
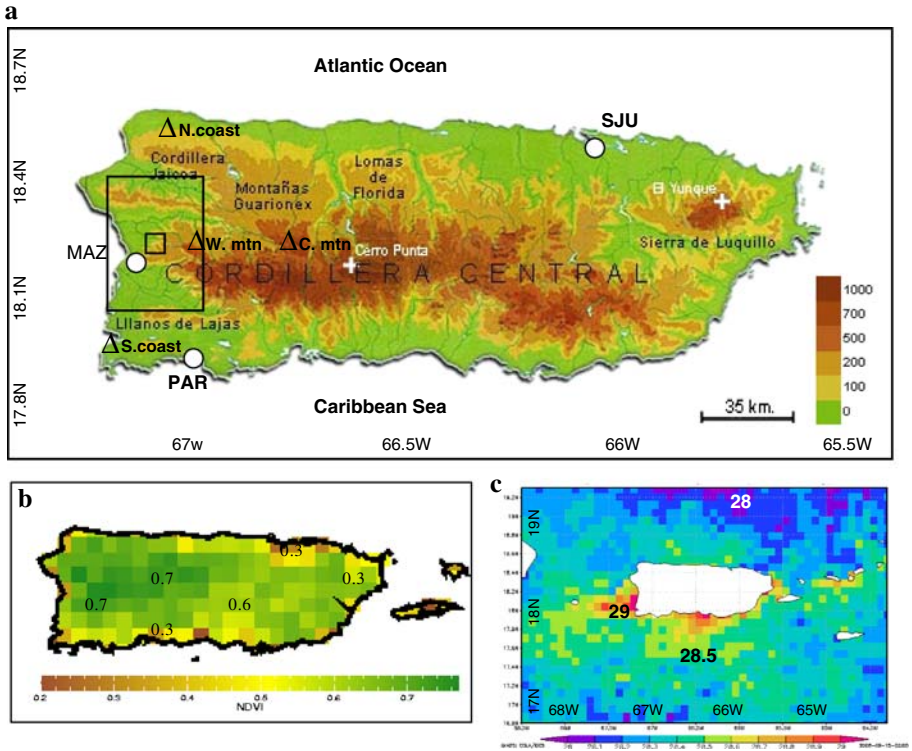
Fig. 1 **a** Topographic map of Puerto Rico, with coastal stations used in the study. The *large open square* is the 'Western box' wherein rain and stream gauges are located, the *smaller open square* is the micro-network, flux stations are shown by *triangles*; **b** mean satellite vegetation index with fraction values; **c** sea-surface temperatures for June–July 2006

Numerous studies have applied mesoscale meteorological models in idealized scenarios and real cases (Bao et al. 2008). The study of Cuxart et al. (2006) for Majorca made use of a high resolution model to simulate the interaction of the island air flow and rain producing clouds. Comparisons were made between model simulations, weather radar and satellite images, and surface observations. Similar work was done for Long Island, NY, USA (Colle and Yuter 2006). More theoretical studies have made use of models for the simulation of the mean state or a specific type of weather. A single-layer hydrostatic and a three-dimensional (3D) non-hydrostatic model were used to represent wakes from the island of St. Vincent in the eastern Caribbean (Smith et al. 1997). Such an island wake can deliver turbulence downstream depending on conditions in the ABL. The Froude number is used to compare mountain height, wind shear and thermal stability, and to determine whether the downstream turbulence will be organized or dissipative. Wakes have been analyzed using ship-based weather radar data leeward from the Hawaiian Islands, in conjunction with mesoscale model simulations (Burk et al. 2002). Smolarkiewicz et al. (1988) and Rasmussen et al. (1989) found that cloud bands over the Hawaiian Islands tend to form either upstream or alongside the island. There, a strong inversion results in trade winds being blocked by the tall mountains, so west coasts are dry.

Our study is motivated by the increasing demand for fine scale and more accurate short-range (1–3 h) weather forecasts of rapid convective initiation and localized flooding. It makes use of the Weather and Research Forecasting (WRF) model in a sub-tropical island setting. Pagowski et al. (2005) evaluated the WRF model for its ability to simulate changes in ABL and land-surface fluxes under a variety of atmospheric conditions. Recent studies have demonstrated that ABL schemes used in the WRF model exhibit scale dependence with respect to diurnal amplitude and weather type (Chiao 2006). The Yonsei University (YSU) and the Mellor–Yamada–Janjic (MYJ) schemes have been compared, and for dry conditions, the YSU ABL is shallower than that from MYJ.

Our primary focus is: (i) to describe the mesoscale structure of Puerto Rico's wind field and diurnal convection; (ii) to better understand ABL transformation in flow passing over a mountainous vegetated island; (iii) to consider what is required to better verify a mesoscale model's ability to represent island-scale weather. We hypothesize that both sea-breeze confluence and a mountain wake play important roles in forcing the local convection. To achieve our objectives we compare WRF model simulations with the available observations. Across Puerto Rico there is a network of ≈20 second-order stations that make routine and automated weather measurements, and there is a National Weather Service (NWS) forecast office with Doppler weather radar and radiosonde profiles. This part of the Caribbean is within the North American reanalysis and forecasting domain covered by high-resolution models that assimilate the available data to a horizontal grid of ≈12 km, thus making it possible to study the mesoscale structure of trade wind convection over the island. In Sect. 2 the data and analysis methods are outlined, and Sect. 3 provides the results, divided into climatology, diurnal cycle, composite results, case studies and numerical simulation. Section 4 is a comparative discussion, and in Sect. 5 we summarize the results and offer recommendations for further work.

2 Data and Analysis Methods

The island topography of Puerto Rico is shown in Fig. 1a, wherein the larger inset box over the western plains contains a distributed network of nine rain gauges and three streamflow gauges maintained by the National Weather Service (NWS) and US Geological Survey (USGS), while the University of Puerto Rico Mayaguez maintains a network of 16 automatic gauges that provide information on rain rate (smaller inset box). Hourly METAR (i.e., meteorological terminal air report) observations are made at Mayaguez regional airport, and are helpful in describing the west coast sea breeze. The Department of Nature Conservation maintains a network of automatic weather stations that measure radiation fluxes, soil moisture, air temperature and humidity, and here we analyze surface data from four sites in western Puerto Rico (triangles in Fig. 1a) to estimate surface heat fluxes. Radiosondes are launched at 12-h intervals at the upwind location of San Juan, and the profiles are used to quantify the atmospheric stability and wind shear. All of these local data are assimilated by the National Centers for Environmental Prediction (NCEP), together with satellite, aircraft, ship, buoy and ancillary data, to provide the observational density required to understand mesoscale phenomena over Puerto Rico.

We make use of satellite data to quantify the mesoscale structure of rainfall and cloud features over Puerto Rico. Comparisons between various products and our local gauge network revealed that the cMorph multi-satellite product (Joyce et al. 2004) was superior to others (e.g., GPCP, TRMM); these data are available every three hours at 25-km resolution and we extract a time series for the 'Western box'. We analyzed the island's summer climate

using North American reanalysis data (NARR), a 32-km assimilation of all available data by a 29-level mesoscale numerical weather prediction model (Mesinger et al. 2006). This dataset represents the island-scale pattern of temperature and winds compared with the coarser NCEP reanalysis products (10 grid points vs. 1), but is known to have a dry bias in the Caribbean (Jury 2009). Here we analyze the mean NARR wind field, geopotential thickness, sea-level pressure, and absolute vorticity at low levels over Puerto Rico for the month of July 2006. We chose this month as representative of mid-summer when terrestrial heating is maximum, trade winds are strong, and synoptic disturbances such as westerly troughs and hurricanes are infrequent. We also analyze the mean diurnal cycle as time-height plots at Mayaguez and as time-latitude or longitude sections across Puerto Rico. Because we are interested in the initiation of convection as the sea breeze forms and the ABL deepens, we analyze data for 0500–2100 LST. In addition to the satellite rainfall data, we also extracted satellite vegetation (NDVI) and SST data and calculated the July 2006 mean fields.

Three-hourly cMorph satellite rainfall data available for the period 2005–2007 over a 200×400 km domain around Puerto Rico (17–19.1°N, 68.5–64.5°W) were subjected to singular value decomposition (SVD) to identify any 'island mode'. SVD involves an eigenvector decomposition of the covariance matrix within a single input field, so the variability is reduced to modes of descending normalized variance (see http://iridl.ldeo.columbia.edu/dochelp/StatTutorial/SVD/ for further details). For each mode there is a spatial cluster (loading) and a series of expansion coefficients (time scores) that describe its fluctuation (Bretherton et al. 1992; Enfield and Alfaro 1999; Chang and Saravanan 2001). The goal here is to characterize the pattern of mesoscale variability, and to distinguish afternoon, island-only rainfall from marine signals. We examined the dominant loading maps and their SVD time scores. Modes 1, 2, and 3 have uniform or dipole structures over the ocean, whilst mode 4 is concentrated over the western interior of Puerto Rico during afternoon hours (the island mode) with negative loading over the surrounding ocean. We repeated the SVD analysis with varimax rotation, but found little change; we also calculated the mean annual and diurnal cycles for the island mode. Upon considering the diurnal cycle, we extracted the peak time (1400–1700 LST) SVD scores together with radiosonde 850-hPa wind direction and Froude number ($F = U/N\,h$, where U is the upstream wind component, N is the upstream Brunt–Vaisala frequency $= (g/\theta)(\partial\theta_v/\partial z)^{1/2}$, and h is the averaged mountain height $\approx$600 m). Cases of trade wind convection over the island were selected when (i) the island mode SVD score ranked in the upper tercile (hence afternoon rainfall confined to the island), (ii) the 850-hPa wind direction was 090° ± 15° (easterly), and (iii) the Froude number (F) was 0.95 ± 0.2. This range of F indicates that the flow passes over Puerto Rico while experiencing orographic modulation. Applying these criteria to the summer of 2006, we found ten cases to include in a composite analysis: 15 May, 27 May, 27 June, 2 July, 17 July, 20 July, 18 August, 30 August, 22 September, and 26 September; and mapped the meteorological fields for these days using the NARR data. Similarly we calculated the composite average of cMorph rainfall and Mayaguez hourly observations for the ten days meeting the above criteria. These data, being space-time averages, tend to smooth or under-represent processes occurring within thunderstorms.

Infrared satellite images were extracted from the National Aeronautics and Space Administration (NASA) website via http://disc.sci.gsfc.nasa.gov for the case study days and some examples are presented. The 22 September case had a CloudSat overpass at 1400 LST, so the vertical structure of reflectivity was extracted for a north-south slice over Puerto Rico. Tropical Rainfall Monitoring Mission (TRMM) satellite data were analyzed for cloud vertical structure during July 2006, and 12-km resolution operational Weather Research and

Forecasting (WRF) model analyses were drawn from NCEP archives via the NOMADS website.

Statistical analyses use the correlation of the daily time series of rainfall, streamflow, and various weather indices drawn from National Climatic Data Center (NCDC) surface and radiosonde archives (CARDS). Upon consideration of the annual cycle of cMorph rainfall SVD time scores, we chose the period 1 May–30 September 2006 as the mid-summer window for statistical analyses. Variables include the cMorph rainfall over the western box, the nine-gauge observed rainfall in the western box, the three-gauge average streamflow, the change in streamflow from one day to the next, the surface zonal wind component at Mayaguez airport from 1100 to 1300 LST, the 700-hPa dewpoint depression and Froude number from the morning (0800 LST) San Juan radiosonde. Although the sample size is 151 days, persistence brings the degrees of freedom to $\approx$50 such that $r \geq |0.23|$ is significant at the 90% confidence limit. To study the interrelationships and bias we scatter-plot certain pairs of variables including: streamflow and rainfall, and cloud efficiency (rainfall divided by precipitable water) versus the standard deviation of gauge rainfall (spatial heterogeneity). To summarize, pre-existing observations are used to study the mesoscale structure of trade wind convection over Puerto Rico. We analyze operational and local datasets for mesoscale features and we simulate some of the cases using a high resolution version of the WRF model as outlined below.

2.1 Modelling of June 27 and July 20 Cases

Numerical simulations are performed using the Advanced Research version 2.2 of WRF; detailed information on the WRF model may be found at: http://www.wrf-model.org. Our simulations are configured with an outer domain that includes $\approx$100 km of ocean all around the island. A total of 51 unequally spaced layers in the vertical were employed with the lowest model level 10 m above ground and the uppermost at 50 hPa. The model was initialized with four-dimensional GFS (Global Forecast System) 0.5 degree, 3-hourly data from NCEP. The model had 18 h of spin-up time prior to convection. Radiosonde profiles at San Juan provide additional input to the WRF model, and also enable calculation of the Froude number. The YSU ABL scheme is employed that permits non-local mixing, entrainment of heat, moisture and momentum, as well as counter-gradient transport (Hong and Dudhia 2003). The WRF atmospheric radiation scheme accounts for longwave and shortwave transfer and interactions within the atmosphere, clouds and surface (Mlawer et al. 1997). No cumulus parameterization is used; precipitation is produced from grid-scale condensation and convection determined from an explicit moisture scheme that includes ice phase microphysics (the WRF single-moment 3-class ice scheme). The atmospheric component is coupled to a land-surface model (Mitchell et al. 2002) that includes four soil layers, and solves the water and energy balance equations at the land surface; the Noah land-surface model (LSM) is employed here (Rogers et al. 2001; Ek et al. 2003; De Haan et al. 2007).

We employed a nested-grid with outer and inner domains of 3-km resolution (160×84 grid points) and 1-km resolution (272×109 grid points), respectively. Although quantitative analyses are possible, here we focus on qualitative interpretations made by comparing model simulated and observed fields. The processes underlying island-scale convection were evaluated from 1-km resolution WRF fields of low-level winds, specific humidity, potential vorticity and vertical velocity. We investigate the spatial structure of prevailing easterly winds across the island, and how these affect ABL height (defined by lapse rate and turbulence) and afternoon convection for two summer cases. Although model data are available at hourly intervals, for brevity we present early afternoon fields to focus on the initiation of convection.

Observations specific to the two simulated cases include automatic weather station data on the north-east coast at San Juan, 'downwind' on the south coast at Parguera, and 'leeward' on the west coast at Mayaguez (cf. Fig. 1a).

3 Results

3.1 Climatology of Convection and Circulation

Many studies have documented the development of summer convection in the Caribbean (Malkus 1954) between May and October that follows the solar angle and trend of SST (Enfield and Alfaro 1999; Giannini et al. 2000; Chen and Taylor 2002). While the early and late summer rains derive from westerly troughs and tropical cyclones, it is the mid-summer rains that maintain water supplies and agriculture in the face of high evaporation. Trade winds strengthen in June–July as the main North Atlantic anticyclone extends a ridge westward into the Caribbean (Amador 1998; Jury et al. 2007; Muñoz et al. 2008). The frequency distribution for observed rainfall (Fig. 2a) indicates that, on 33% of rain days the area-average over western Puerto Rico is $\leq 2\,\mathrm{mm\,day^{-1}}$. Another 33% of rain days are in the 'beneficial range' 3–8 mm day^{-1} (the mean value), while the upper tail of the distribution is made up of externally forced weather events that contribute to local flooding and soil erosion.

The frequency distribution of zonal wind from daytime observations at Mayaguez in 2006 is presented in Fig. 2b; there is a high percentage of easterly winds ($U < 0$) as expected, yet a westerly sea breeze ($+2$ to $+4\,\mathrm{m\,s^{-1}}$) occurs about 33% of the time throughout the year. Cross-correlation of the observed rainfall time series and the zonal wind at Mayaguez over the period May to September 2006 was found to be insignificant ($r = +0.08$) but higher with respect to streamflow with $r = +0.21$. Although somewhat puzzling, we found that the sea breeze is ubiquitous due to high diurnal heating, whereas rainfall is naturally intermittent. Streamflow, on the other hand, is continuous and represents a spatial aggregate. Hence sea breezes that converge with trade winds contribute to enhanced run-off, see later. The correlation between rainfall and the 700-hPa dewpoint depression ($r = -0.23$) indicates that subsidence above the trade-wind inversion is a constraint on convection.

The Froude number has little bearing on western Puerto Rico rainfall ($r = -0.08$) but has some impact on streamflow ($r = -0.27$). A decrease in the Froude number arises when the trade winds diminish, since the lapse rate in the ABL remains approximately moist adiabatic. Very weak winds coincide with lower pressure and widespread clouds that dampen the diurnal cycle, while moderate easterly flow ($8\,\mathrm{m\,s^{-1}}$) gives sufficient time (6-h) for surface heating to affect ABL structure across the island.

The scatter-plot of cloud efficiency and rainfall heterogeneity (standard deviation amongst nine gauges) is given in Fig. 2c, where we see a monotonic increase in the ability of clouds to convert precipitable water to rainfall as the spatial distribution becomes more 'patchy'. This is expected, and as cumulus clouds develop into thunderstorms they become more isolated. The linear regression fit is high ($r^2 = 81\%$). Figure 2d illustrates the scatter-plot of observed rainfall and streamflow both averaged over the western box (Fig. 1a) for the 2005–2007 period. River basins in Puerto Rico are small and their response to run-off is rapid, so simultaneous correlations are superior to a lag of one day ($r^2 = 51\%$).

We objectively analyzed island-scale rainfall via SVD applied to three-hourly satellite rainfall in the period 2005–2007 (sample size >5000). The island mode SVD scores averaged over the diurnal cycle (Fig. 3a) reveal that the amplitude peaks from 1100 to 1700 LST over the island (Fig. 3c) in agreement with Carter and Elsner (1997). The marine mode, on
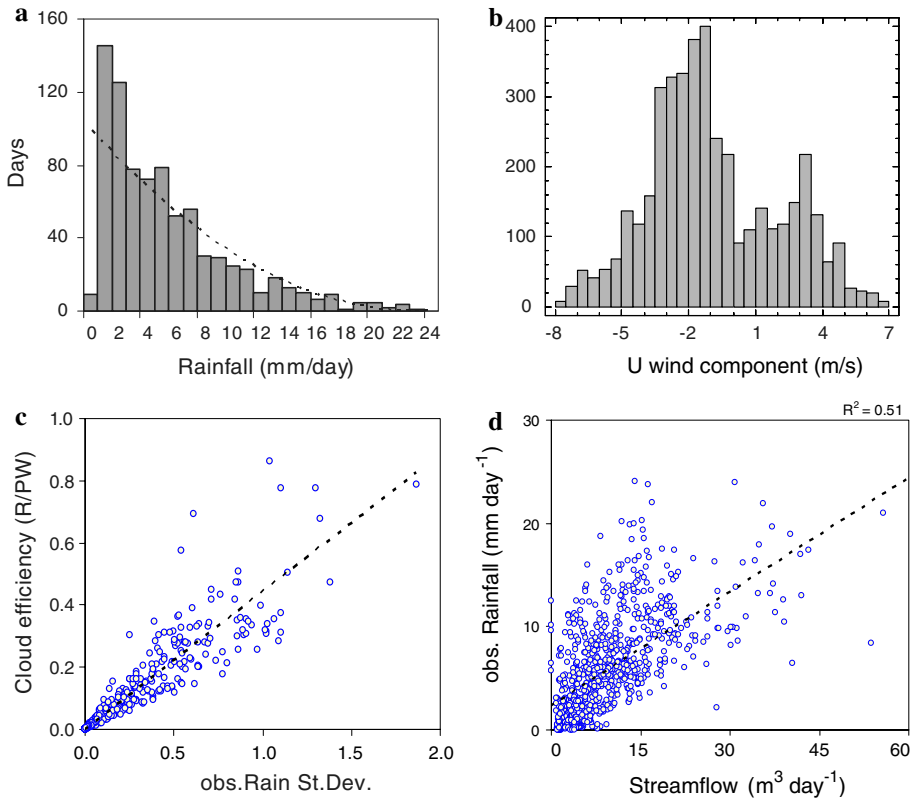
Fig. 2 **a** Frequency distribution for observed rainfall with rain $\leq 2\,\mathrm{mm\,day^{-1}}$ 34%; **b** frequency distribution of 10 m zonal wind in 2006 from hourly daytime observations at Mayaguez; **c** scatterplot of cloud efficiency versus rainfall heterogeneity (sigma); **d** scatterplot of rainfall versus streamflow; all based on daily data in 2006 in the Western box (Fig. 1b). *Regression lines* are fitted

the other hand, is at a minimum from 0800 to 1400 LST and has little diurnal amplitude, as expected. Its spatial loading is evenly distributed across the domain, with a slight preference for the Caribbean sector (not shown). We interpret the marine mode as one that is synoptically forced by mobile westerly troughs and easterly waves, whose scales and dynamics are largely unaffected by the island. The annual cycle of SVD scores averaged over three years reveals interesting features. The marine mode (not shown) follows the annual cycle of SST around Puerto Rico, while the island mode (Fig. 3b) rises from May to August then declines, tracking the solar angle and terrestrial heat fluxes more closely. The variance explained by the marine mode is 25%, compared with 6% for the island mode. Based on a ranking of the island-mode SVD scores in the period May to September 2006, together with radiosonde profile data, a group of ten days were selected for composite averaging as outlined in Sects. 2 and 3.3.

We analyzed the background circulation using NARR analyses for July 2006. The mean surface wind (Fig. 4a) is easterly, but there is an 'island footprint' represented by a band of lower wind speeds stretching across Puerto Rico, and halved immediately west of the island: a wind shadow (Bennet et al. 1998). Higher wind speeds ($\approx 10\,\mathrm{m\,s^{-1}}$) are found $\approx 60\,\mathrm{km}$ to the north and south of the island. The absolute vorticity field has a marked north-south

Fig. 3 SVD analysis of three-hourly satellite rainfall in the period 2005–2007. **a** Time scores averaged over the diurnal cycle in 2006; **b** SVD scores averaged over three annual cycles, overlain with 2nd order trend to reflect solar flux. Spatial loading pattern for island mode rainfall; **c** first three modes not shown. SVD scale is −3 to +3σ from cool to warm *colours*. *Dashed lines* in **c** refer to sections analyzed in Fig. 5
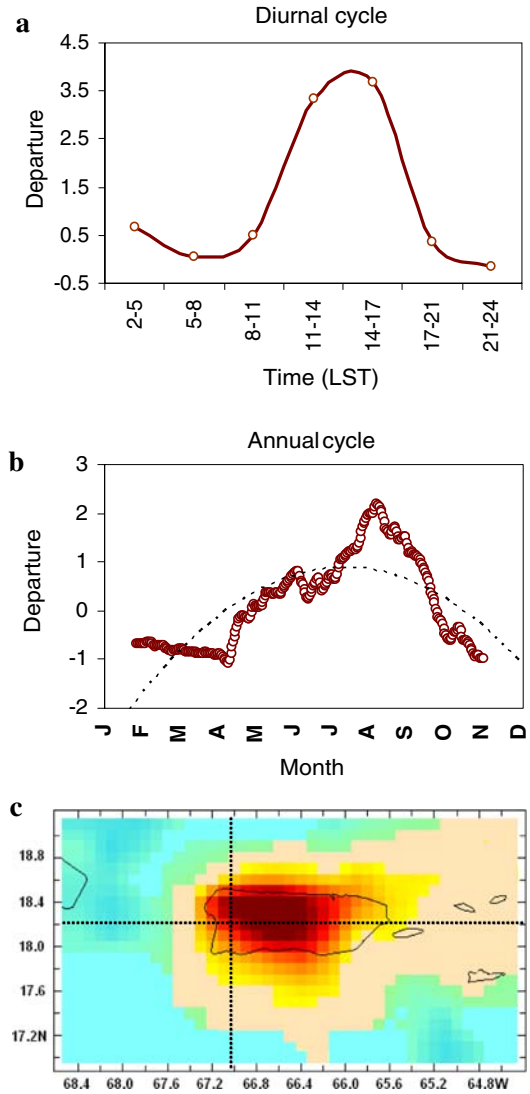
dipole pattern, and cyclonic (anti-cyclonic) shear and curvature is found off the north-west (south) coast indicative of two counter-rotating gyres of radius ≈30 km. The NARR sea-level pressure (SLP) and 1,000–500 hPa geopotential thickness field for 1400 LST averaged for the month of July 2006 are given in Fig. 4b. At night mesoscale structures are weak (not shown), but the afternoon field reveals an island footprint in the SLP and thickness fields. There is a surface pressure trough extending northward from the Caribbean along the west coast of Puerto Rico. The thickness field reflects a thermal low over the western interior of the island with a radius of 30 km centered on 18.2°N, 66.9°W.
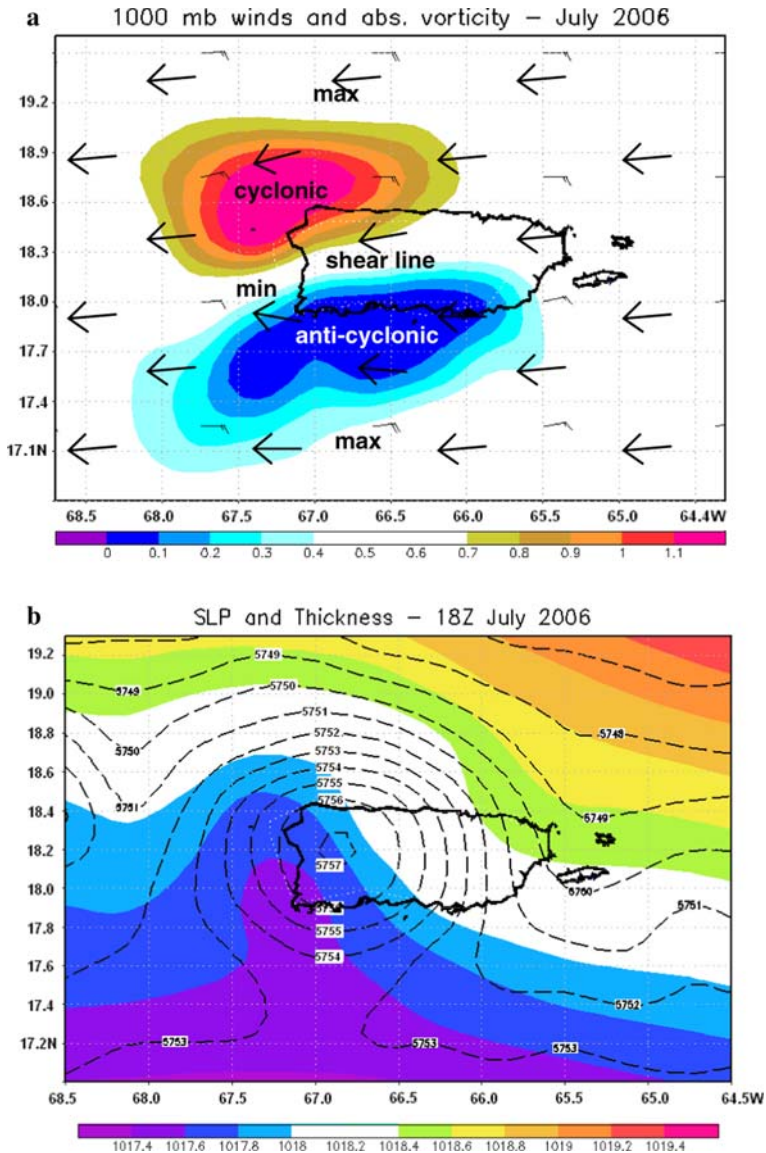
Fig. 4 **a** NARR July 2006 surface wind (*barbs/arrows*, max/min) and absolute vorticity ($10^{-5}\,\mathrm{s}^{-1}$, *shaded*); **b** sea-level pressure (*shaded* hPa) and 1,000–500 hPa geopotential thickness (m, *dashed contours*) at 1400 LST with lee-side trough

3.2 The Diurnal Cycle: July 2006

As reported earlier, shallow short-lived afternoon thunderstorms are a regular feature of summer weather over western Puerto Rico, but their location and intensity are highly variable and make operational forecasting quite challenging. The diurnal cycle has distinct phases: the first phase is from sunrise until the sea breeze reaches maximum intensity coincident with

high solar radiation; the second phase concerns the development of cumulonimbus clusters along shear lines and short periods of rainfall; while the final phase involves irregular decay of the ABL and nocturnal recovery. We will focus on the ABL growth phase from sunrise to convective initiation using NARR reanalysis fields and local observations.

We analyze NARR data over the diurnal cycle from 0200 to 1700 LST averaged for July 2006; the time-height cross-section of zonal wind and 850-hPa vertical motion near Maya-guez is illustrated in Fig. 5a. A layer of strong trade winds prevails from 1 to 1.5 km and extends to the surface before sunrise at 0500 LST (blue shading). After sunrise a turbulent surface layer develops as represented by a decrease in the easterly flow after 0800 LST (orange shading). According to the NARR, thermally weakened easterlies reach a height of 800 m by 1400 LST, before subsiding. The vertical motion field indicates sinking in the 500-m layer around 0500 LST and rising motion in the 1–1.5 km layer at 1400 LST. Hence the NARR 32-km analysis does not identify the reversal of winds over the west coast that is frequently observed (cf. Fig. 2b).

The vertical structure of cloud properties over the western box in July 2006 is analyzed from TRMM data in Fig. 5b. The latent heating profile reaches a maximum in the 6–8 km layer ($\approx$ freezing level), where afternoon thunderstorm updrafts condense water rapidly. The cloud water content is high in the 2–6 km layer, with highest values just below the trade wind inversion. There is evidence of dry air entrainment above 6 km. Cloud ice concentrations are at a maximum around 10 km, but achieve half the value of cloud water, consistent with observations that indicate that about 33% of rainfall occurs from warm clouds with no thunder reported.

We analyze vertical slices of NARR diurnal data as Hovmoller plots. In Fig. 5c the time-latitude Hovmoller on 67°W of the 925-hPa meridional V wind component and turbulent kinetic energy (TKE) reveals the inward turning of the wind at 17.9° and 18.5°N in the afternoon (1100–1700 LST) coincident with an increase in TKE over the mountains (18.2–18.3°N). This suggests the presence of both mountain wake and sea-breeze confluence. At night and in the early morning, the winds are diffluent along the north and south coasts of the island as cool drainage flows join the prevailing trade winds. The time-longitude Hovmoller on 18.2°N of the ABL height and surface temperature (Fig. 5d) reveals high surface heating and a westward and time-lagged response of the ABL depth similar to idealized simulations of Baik (1992). July 2006 surface temperatures from the NARR analysis peak over the centre of the island from 1100 to 1400 LST. The surface heating is embedded within a persistent trade wind flow, so that the ABL response is lagged in space (30 km) and time (2 h). The ABL grows from 900 to 1,800 m from 0500 to 1400 LST, reaching a maximum near the west coast, consistent with Schafer et al. (2001). The ABL height over western Puerto Rico reduces after 1400 LST as a result of cooling by rain and associated convective outflows, and reduced solar insolation. We investigate the response of winds to diurnal heating as composites and case studies below.

3.3 Composite Structure of 10 Cases

By compositing similar cases, as done by May and Wilczak (1993) and Schafer et al. (2001), we are able to identify mesoscale forcing within the trade wind convection. We have outlined the procedure for case selection involving a hierarchal sorting of the data in the summer of 2006: first by the SVD score, which ensures afternoon rain over the island, then by the 850-hPa wind and Froude number. The 10-case composite cMorph satellite rainfall map for 1100–2100 LST is given in Fig. 6, showing a maximum over the western interior of Puerto Rico. This feature has a radius of 30 km centered on 18.25°N, 66.9°W. The rainfall intensity
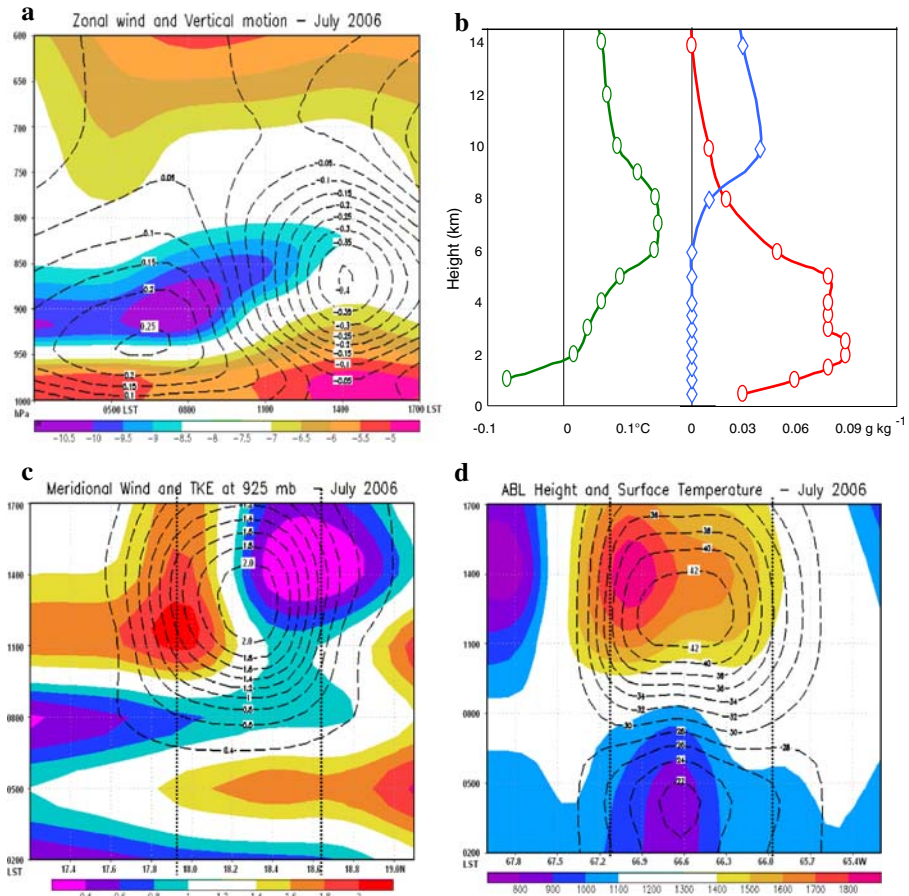
Fig. 5 NARR July 2006 mean **a** time-height cross-section of zonal wind (*shaded*, m s^{-1}) and 850-hPa vertical motion (*dashed lines*, Pa s^{-1}) at Mayaguez; **b** vertical profiles in the Western box for July 2006 of (**b**) latent heating (C day^{-1}) and cloud water and ice (g kg^{-1}); **c** NARR July 2006 mean time-latitude Hovmoller on 67W of 925-hPa *V* wind component (*shaded*, m s^{-1}) and turbulent kinetic energy (*contours*, J kg^{-1}); **d** time-longitude Hovmoller on 18.2N of ABL height (*shaded*, m) and surface temperature (*dashed lines*, °C). Island edges are shown by *thin vertical dotted lines*. Panels c and d are taken on *lines* shown in Fig. 3c

is underestimated by a factor of ≈3. Observations from the 16-gauge network near Mayaguez are given in Table 1, and indicate the average storm lifespan is ≈1500–1700 LST and mean observed rainfall is 11.6 mm (≈5 mm h^{-1}). The composite mean maximum storm-total rainfall is 26.4 mm, the minimum is ≈3 mm, and represents a high degree of spatial variability within a 16 km^2 area, as would be expected for isolated short-lived thunderstorms. The 10-case composite hourly rainfall for the two mountain stations is given in Fig. 6b, and shows a sharp maximum at the central site of 7 mm at 1600 LST, while the western site has lower rainfall, and a peak around 2000 LST. The composite storm displacement is thus westward at ≈10 km h^{-1}.

The growth of the heated convective layer over the southern mountains and western plains is a key factor controlling the potential for convection as outlined earlier by Pearce et al. (1956). The Mayaguez sea breeze is analyzed for the composite group in Fig. 6c and d. Air

Table 1 Statistics for 10 cloud band cases observed from the network of 16 automatic rain-gauges near Mayaguez (small box in Fig. 1a)

16-Gage network	Start LST	Storm end	Dur. (h)	Mean (mm)	Max (mm)	Min (mm)
Avg.	1,456	1,714	2.31	11.6	26.4	3.2
St. dev.	1.6 h	1.7 h	0.93	7.8	13.9	3.2
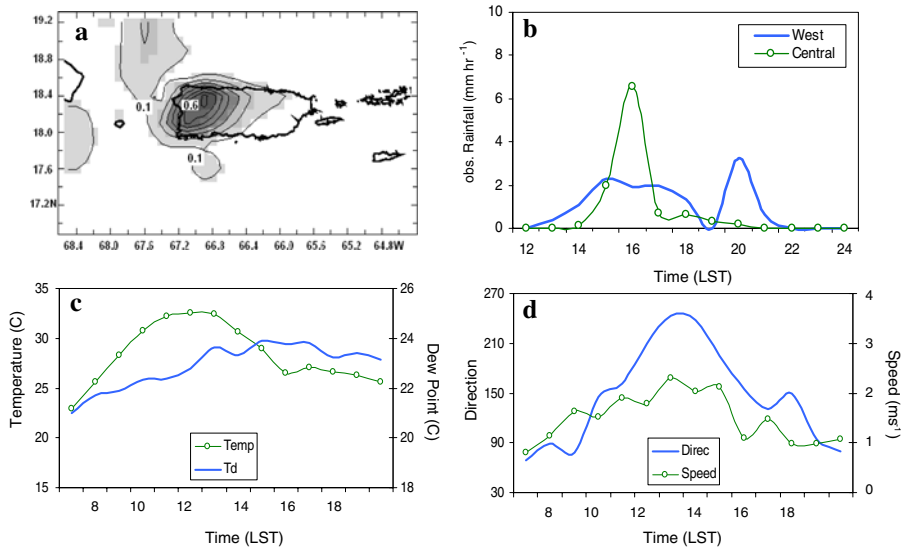
Fig. 6 Ten case composite satellite rainfall map averaged over the period 1100–2100 LST with units mm h^{-1}; **a** composite rainfall in central and west mountain sites; **b** composite 2-m air temperature and dewpoint; **c** 10-m wind direction and wind speed (**c**) at Mayaguez. Time scales vary

temperatures increase from 23°C at 0700 LST to 33°C by 1100 LST, and dewpoints rise in tandem reaching 24°C by 1400 LST. Two factors underpin the rise of dewpoint temperature, (i) moisture advection from warm seas west of the island (cf. Fig. 1c), (ii) a mountain wake enriched by evapotranspiration. The composite wind direction and wind speed at Mayaguez airport show a turning of the wind from morning trade winds to midday sea breeze. This transition is often abrupt, but appears smooth in the composite.

Table 2 provides statistics for each of the ten 'cloud band' cases. The observed mean rainfall is 7.6 mm with a standard deviation of 5.5 mm, and the mean sea-breeze speed at Mayaguez is 2.2 m s^{-1} with a standard deviation of 2.8 m s^{-1}. In two cases the westerly sea breeze was absent, but trade wind confluence still produced localized convection. The 700-hPa mean dewpoint depression is 8.7°C, and the 850-hPa wind at San Juan is 7.8 m s^{-1} from 090° (east) with a 10° standard deviation. The composite Froude number is near unity, with half of the cases around 1.2 and the other around 0.7. The mean convective available potential energy (CAPE) is 1,726 J kg^{-1} as expected during summer in the sub-tropics with SST >28°C (cf. Fig. 1c), and consistent with climatology.

Table 3 provides composite averages of surface meteorological data for the coastal and mountain flux sites (cf. Fig. 1b). At the southern and northern coastal sites, temperatures and wind speeds rise from 22.6 to 30.2°C, and 3.2 to 6.4 m s^{-1} by 1400 LST, respectively.

Table 2 Statistics for the 10 cloud band cases

Date	Est.Rain	Obs.Rain	S.flow	dS.flow	dS.+1	U.maz	700TD	U850	850dir	Froude	CAPE
15-May-06	5.49	13.91	628	174	290.7	5.03	5	−5.51	100	0.66	1818
27-May-06	1.39	5.88	425	245	46	4.07	16	−9.5	90	1.20	913
27-Jun-06	4.23	2.61	319	−173.3	285.6	1.09	10.9	−9.31	100	1.10	1589
02-Jul-06	1.47	10.31	196.7	−71.6	36.3	−0.77	2.4	−10.71	95	1.18	543
17-Jul-06	4.08	1.14	265.7	54.7	7	−4.09	7	−8.89	75	1.13	2229
20-Jul-06	9.90	17.4	349	−112.7	171.7	2.55	11.9	−8.57	80	1.07	2584
18-Aug-06	26.70	10.6	910.3	162.6	470.7	2.84	9	−5.58	95	0.72	1929
30-Aug-06	3.47	5.73	570	301.7	−46.7	4.59	8	−4.03	95	0.60	2296
22-Sep-06	7.32	7.29	665.3	−201.7	−291.3	3.87	13	−5.97	70	0.78	1703
26-Sep-06	6.30	1.02	304.3	−200.7	−298	2.98	10.9	−9.41	85	1.17	1655
Avg.	7.0	7.6	463.3	17.8	67.2	2.2	8.7	−7.8	88.5	0.97	1, 726
St. dev.	7.4	5.5	223.6	193.3	247.5	2.8	3.5	2.2	10.6	0.26	619

Variables are Est.Rain = cMorph average in Mayaguez, Obs.Rain = 9 gauge average (over large box Fig. 1a), S.flow = 3 gauge average streamflow, dS.flow = change in streamflow, dS.+1 = change in streamflow at one day lag, U.maz = midday zonal wind at MAZ, 700TD = 700-hPa dewpoint depression at San Juan, U850 = 850-hPa zonal wind at San Juan, 850dir = 850-wind direction at San Juan, Froude (number) is based on SJU radiosonde. CAPE = convective available potential energy

Wind directions at the northern (southern) site turn to $\approx 50°$ (120°) around midday, providing confluence for thunderstorm formation. Dewpoint temperatures over the coast (mountain) increase by 2°C (5°C). Rainfall of $4.2 \, \text{mm h}^{-1}$ in the 1500–1600 LST period induced soil moisture to rise from 32.1 to 33.4% soon thereafter. Surface fluxes were estimated from the Penman–Monteith equation for vegetated canopies (Allen et al. 2005) and compared with model results. The operational 12 km WRF flux estimates at 1400 LST for the 10-case composite are: $Q_e = 225 \, \text{W m}^{-2}$, $Q_h = 83 \, \text{W m}^{-2}$ (coast) and $Q_e = 224 \, \text{W m}^{-2}$, $Q_h = 57 \, \text{W m}^{-2}$ (mountain). Observations (cf. Table 3) are $Q_e = 318 \, \text{W m}^{-2}$, $Q_h = 51 \, \text{W m}^{-2}$ (coast) and $Q_e = 220 \, \text{W m}^{-2}$, $Q_h = 39 \, \text{W m}^{-2}$ (mountain). So there is reasonable agreement.

3.4 Case Study Features

In this section we analyze features for case study days to provide background to the WRF model simulations. The radar images (not shown) suggest that echoes first develop near Cerro Punta around 1300 LST, and propagate westward while intensifying to $\approx 50 \, \text{dBz}$ by 1500 LST. The echoes spread north-south along the west coast sea-breeze 'front' and weaken after 1700 LST with diurnal cooling. Infrared GOES satellite images at 1500 LST overlain with wind streamlines objectively analyzed from NARR are given in Fig. 7a,b for the two case study days. There is a circular area of convective clouds over western Puerto Rico embedded in confluent trade winds. Cloud tops reach −20°C over a 30-km radius centered on 18.15°N, 67.05°W. A CloudSat reflectivity slice for the case of 22 September running north-south through Puerto Rico at 1400 LST is given in Fig. 7c to illustrate vertical structure. Reflectivity values >40 dBz extend through the 3–7 km layer and extend $\approx$ 20km north-south. cloud tops reach 8 km (−20°C). Application of the Marshall-Palmer relationship $Z = 200R^{1.6}$ yields rainfall $>12 \, \text{mm h}^{-1}$, close to observed values (Table 2).

Observations at Mayaguez give evidence of rapid changes in solar radiation and air temperature as clouds deepened. Rainfall up to $12 \, \text{mm h}^{-1}$ was observed during the afternoon

Table 3 Composite average surface observations at the mountain (MTN) and coastal flux sites (cf. Fig. 1a) for the 10 cloud band cases

Coast	T	Td	DIR-N	DIR-S	SPD	Gust	SM	Q_e	Q_h
0500	23	21.4	120	54	0.3	1	29.4	0	−4
0600	22.7	21.3	99	70	0.4	1.3	29.4	0	−4
0700	22.6	21.1	98	92	0.4	1.2	29.3	0	−3
0800	23.1	20.8	132	85	0.6	2.2	29.3	17	7
0900	26	21.1	86	103	1.5	3.6	29.2	82	18
1000	28.2	21.8	78	115	2	4.4	29.3	155	23
1100	29.2	22.4	67	119	2.5	5.2	29.4	245	37
1200	29.8	23	54	124	2.8	5.6	29.5	328	52
1300	30.1	22.9	51	125	3.2	5.9	29.6	349	63
1400	30.2	23.2	49	121	3.2	6.4	29.6	318	51
1500	29.7	23.3	54	83	3.2	5.7	29.6	265	27
1600	28.8	23.1	69	115	3.2	5.9	29.8	184	7
1700	28.3	23.1	77	95	2.9	5.9	30	104	−12
1800	27.2	22.8	93	67	1.9	4.3	31.2	60	−21
1900	27	22.6	90	74	1.4	3.5	31.8	34	−27
2000	26.7	22.7	87	90	1.5	3.8	31.5	1	−27

MTN	PCP	T	Td	DIR	SPD	Gust	SM	Q_e	Q_h
0500	0	19	17.1	182	0.9	2.6	32.4	1	0
0600	0	19.1	17.4	149	1	2.9	32.3	1	0
0700	0.02	19	17.4	142	1	2.9	32.4	1	0
0800	0	19.2	17.4	163	0.9	2.7	32.5	8	2
0900	0	19.9	17.6	140	0.8	2.8	32.4	27	8
1000	0	21	18.4	158	0.7	2.6	32.3	100	26
1100	0	22.6	19.1	163	0.7	2.6	32.4	259	58
1200	0	24.1	20.4	165	0.6	2.4	32.1	280	54
1300	0.21	24.8	21.4	199	0.6	2.6	32.1	289	49
1400	0.6	24.4	22.3	176	0.9	2.8	32.2	220	39
1500	2.14	23.3	21.8	158	1.2	3.3	32.1	135	23
1600	4.22	21.5	20.8	158	1.4	3.9	32.5	48	5
1700	1.37	20.4	20	144	1.3	3.3	32.7	41	6
1800	1.02	20.4	20	162	1	3.1	33	47	6
1900	0.17	20.5	20.2	164	0.7	2.2	33.4	38	4
2000	1.71	20.2	20.1	168	0.6	2.3	33.4	10	−1

Variables are PCP = precipitation (mm h^{-1}) at MTN sites, T = temperature (°C), Td = dewpoint (°C), DIR = wind direction, N = north coast site, S = south coast site, SPD = speed (m s^{-1}), Gust, SM = soil water fraction (%), Q_e = latent heat flux (W m^{-2}), Q_h = sensible heat flux (W m^{-2})

hours, greater in the 20 July case than on 27 June, as expected from higher CAPE. Afternoon totals up to 42 and 71 mm were recorded in the western mountains on 27 June and 20 July respectively, and stream flows doubled. At Mayaguez air temperatures and dewpoints rose to 32 and 24°C respectively, as the sea-breeze wind speeds reached 6 m s^{-1}. The sea breeze was short-lived (stronger) in the 27 June (20 July) case, and solar insolation peaked at 1200 LST on 20 July before collapsing (Fig. 7d).

Figure 8a and b is the observed and WRF simulated 0800 LST (morning) soundings for San Juan. The model soundings were adequate except for the two warm dry layers around 450 and 700 hPa, and CAPE values determined by the model were 567–849 J kg^{-1} below observed. Both soundings had a wind shift in the 500–600 hPa level from low-level easterlies to weak upper flow. With lower CAPE, we anticipate that the model-simulated rainfall to be less than observed.

Station observations are provided in Fig. 8c and d for the 20 July case, and derive from the upwind and downwind coasts. The SJU site observed easterly winds of 6 m s^{-1} that peaked around 1300 LST, while the PAR site had south-easterly winds of 4 m s^{-1} with a decline around 1400 LST. Thus winds are convergent during midday heating. The temperature and pressure variations were typical of trade wind weather except for the PAR site at 1400 LST when passing convection induced a 6°C cooling, a pressure rise of 1 hPa and a wind direction switch from south to east within 30 min.

3.5 Simulation Results

Figure 9 shows the WRF model simulated radar reflectivity and 10-m wind field for 27 June and 20 July 2006 at 1400, 1500 and 1600 LST. The simulated echoes were similar in intensity (40–50 dBz max) and areal extent compared favorably with radar reflectivity and cMorph estimates (not shown). The model correctly simulated the cloud band on 27 June, but predicted the 20 July cloud band to develop over Mayaguez, when it was observed to be more southerly. The model correctly simulated the westward spread of the cloud band from the central mountains, and the wrapping of the wind flow around the western end of the island in response to diurnal heating and orography.

The WRF model-simulated water vapour mixing ratio, 850-hPa winds and potential vorticity are illustrated for 27 June and 20 July cases in Fig. 10a–d. The water vapour fields at 1100 LST give evidence of evapotranspiration as an important element fueling the cloud bands. Streaks of water vapour were simulated to rise off the vegetated mountains (cf. Fig. 1b) during daytime heating. Many of the streaks had a fetch >100 km wherein the water vapour content increases westward from 10 to 14 g kg^{-1}. The moist plumes rise over the heated surface of the island and are drawn into the western cloud band. The WRF model 1000-hPa potential vorticity at 1400 LST indicates how the trade wind shear divides along the central mountains, producing a positive–negative dipole pattern. Diurnal heating induces the airflow onto the island and the mountain wake (line of negative potential vorticity) aids the convection.

Figure 11 is a vertical east-west section across Puerto Rico of WRF simulated $U-W$ wind vectors and radar reflectivity for 1400 and 1500 LST, and specific humidity for 27 June on a northern line and for 20 July on a southern line. The radar reflectivity values exceed 40 dBz over a layer from the surface up to 8 km from 10 to 50 km inland from the west coast. The vertical growth of reflectivity maxima was from 3 to 7 km from 1400 to 1500 LST on 27 June. The upper portion of the thunderstorm was simulated to reach temperatures of −50°C on both days, thus ice phase processes were brought into play, consistent with observations of thunder and lightning. Our reflectivity structures differ from Szumowski et al. (1997); here convection extends freely through the troposphere, whereas in Hawaii echoes >50 dBZ are trapped below the subsidence inversion. CAPE values in Hawaii are typically < 200 J kg^{-1} in contrast with Puerto Rican values >1000 J kg^{-1}. The WRF simulated specific humidity structure was stratified and had maxima on the east and west coasts. The penetration of the anvil into the upper westerly flow is evident in Fig. 11 for 20 July. Convection over western

Fig. 7 Infrared satellite images for 27 June (**a**) and 20 July (**b**) cases at 1500 LST, with NARR wind streamlines; **c** CloudSat reflectivity slice for the case of 22 September (radar dBz colour-scale >30 *blue*, >40 *yellow*, >50 *red*); **d** Mayaguez 15-min observations of radiation (*orange*) temperature (*solid*) and dew point for 20 July
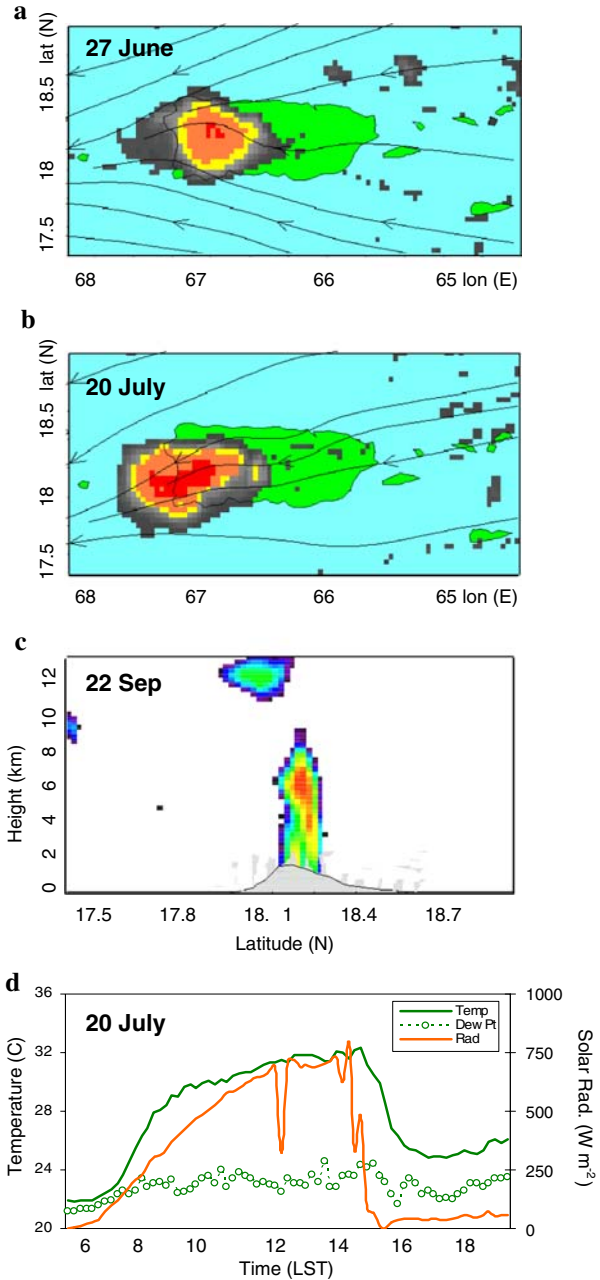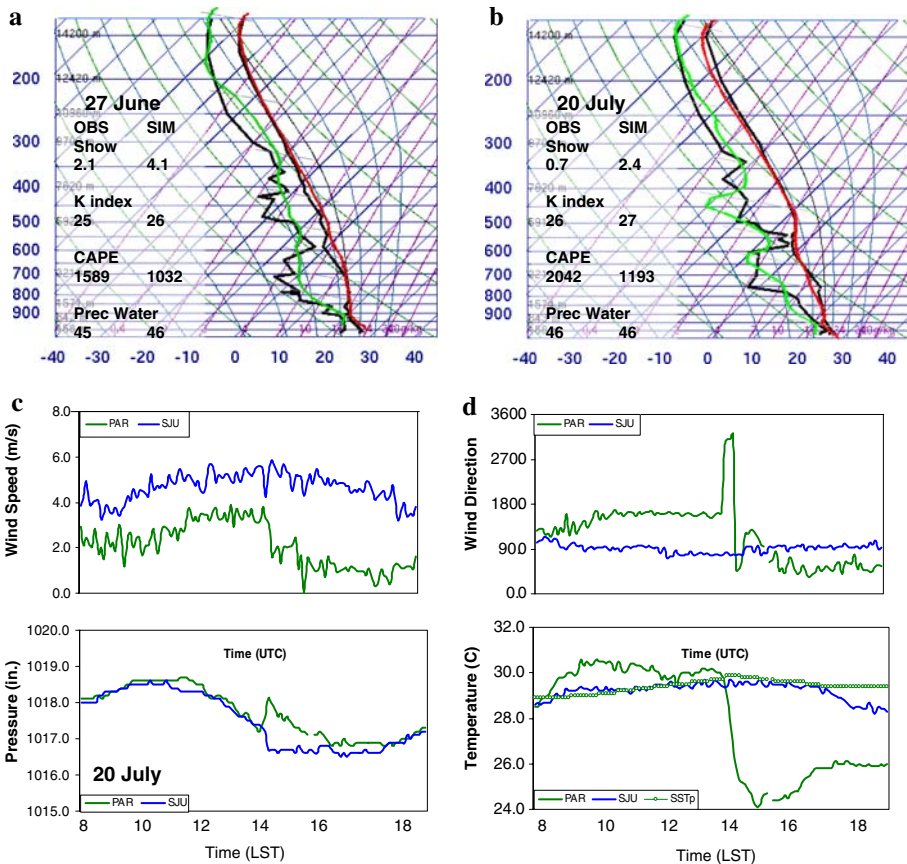
Fig. 8 Radiosonde profiles at 0800 LST over San Juan (*upper*) with WRF sounding over-plotted in *green/red* with thermodynamic indices inset for 27 June (**a**) and 20 July (**b**). Meteorological surface data for 20 July from San Juan (SJU—*blue*) and Parguera (PAR—green), illustrating mesoscale variability (**c, d**). A thunderstorm passed PAR causing increased pressure, wind rotation, decreased temperature and wind speed

Puerto Rico forced moisture upwards ($6\,\mathrm{g\,kg^{-1}}$ reached $5\,\mathrm{km}$), though the thunderstorms weaken rapidly after 1600 LST.

Overall, the explosion of afternoon convection over the western side of Puerto Rico is well simulated by the WRF model. Sensitivity experiments with cumulus parameterization, different land surface and ABL schemes, and different horizontal and vertical resolutions (1 and 3 km; 27, 31 and 51 layers) did not appreciably affect the model's ability to handle Mayaguez thunderstorms during trade winds. In comparison with the 12-km operational WRF model forecasts, we found a significant increase in localized rainfall using 1-km and 3-km horizontal resolutions, mainly near the intersection of the west coast sea breeze and mountain wake.

4 Comparisons and Discussion

One of the aims of our study is to evaluate changes in ABL height contributing to afternoon convection. Results for different stages of the diurnal cycle (cf. Fig. 5c) reveal a uniform ABL
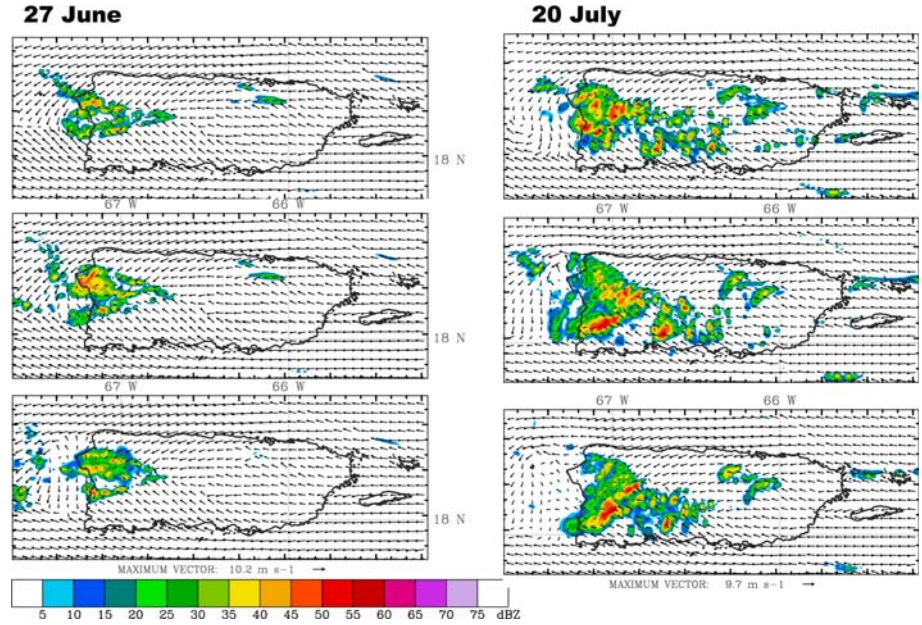
Fig. 9 WRF simulated 10-m winds and radar reflectivity at 1400, 1500 and 1600 LST (*top-down*) for 27 June (*left*) and 20 July 2006 (*right*)
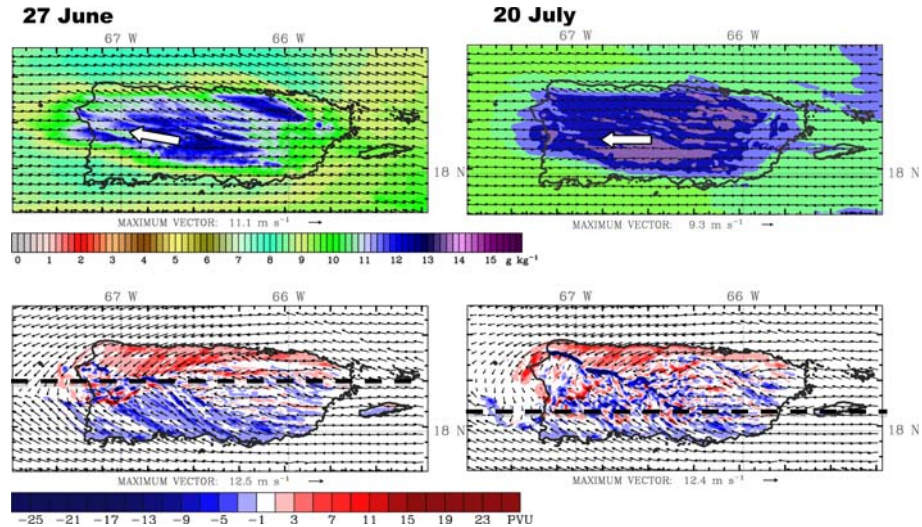
Fig. 10 *Top* WRF simulated specific humidity and winds at 850 hPa for 1100 LST illustrating moisture loading by surface fluxes. *Lower* WRF simulated 10-m winds and potential vorticity at 1400 LST for 27 June (*left*) and 20 July 2006 (*right*). *Dashed lines* identify cross-sections in Fig. 11, *arrows* indicate mean wind direction

of ≈ 300 m during the night and early morning, with rapid growth after 0800 LST. The WRF model simulates an increase in ABL to 2,000 m over the western interior, yet over the sea west of the island, the ABL is <600 m deep. Hence the Cerro Punta wake extends to Mayaguez, but
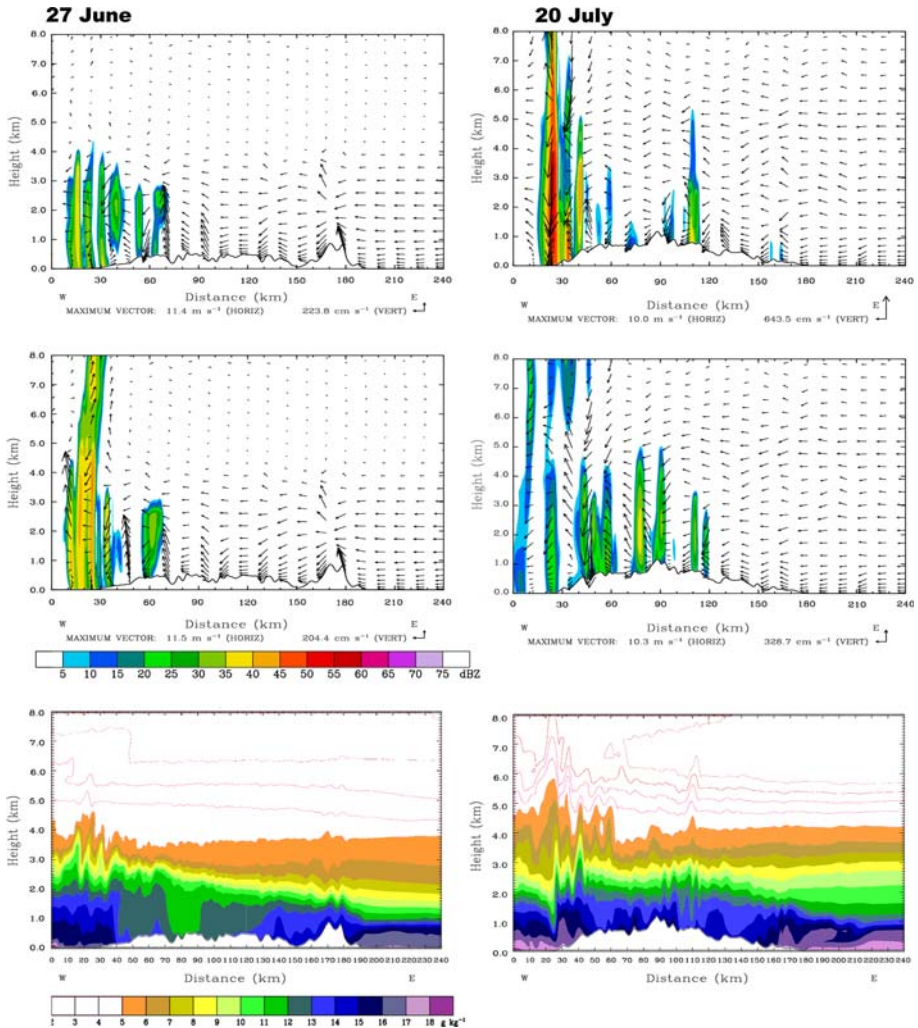
Fig. 11 WRF simulated $U-W$ wind components and radar reflectivity (*top* 1400 LST/*middle* 1500 LST), and specific humidity (*lower*) at 1400 LST on an east-west section over the northern line for 27 June (*left*) and over the southern line for 20 July case (*right*). Vertical scale is 15 times horizontal

is constrained from further extension by the in-folded sea breeze. Our 1-km WRF simulation provides additional detail in comparison to the NARR analysis: there is a 'bow wave' pattern from the island's imprint on the trade wind flow. Over the central mountains and western coastal plains, the streamlines form confluent lines that feed the afternoon thunderstorm. There was little evidence of flow splitting over the island, rather a reduction in momentum. The west coast sea breeze occurs between two counter-rotating gyres connected with trade winds sweeping along the north and south coast. The simulated sea breeze ≈290° at 5 m s^{-1} was consistent with observations. South coast flow was simulated to have a direction from ≈130°, compared with an observed direction of 160°. In our two featured cases the 850-hPa humidity rose to ≈90% over the western coastal plains where surface temperature and

dew-point were 33°C and 24°C, respectively. The WRF model had the 27 June confluence line north of Mayaguez and the 20 July confluence line to the south, in agreement with satellite and radar observations.

To characterize mountain wake formation, the Froude number was evaluated as in Smith et al. (1997) and Jiang and Doyle (2008). In Burk et al. (2002) a number of mesoscale simulations were performed with a strong subsidence inversion that intersects the taller Hawaiian Islands ($F < 0.3$) producing wakes that extend well downstream (Hafner and Xie 2003). In our study, Puerto Rico lies relatively further west in the ocean basin and the subsidence inversion remains above the mountain. With $F \approx 1$, horizontally-trapped vertically-undulating lee waves arise not far downstream (cf. Fig. 11). The ABL has a moist adiabatic lapse rate and persistent easterly flow 2 km deep (H). With a mountain length (L) scale $\approx 10^5$m and a terrestrial drag coefficient $C_D \approx 5 \times 10^{-3}$, the Reynolds number ($H/(C_D L)$) is approximately 4, so a short meandering wake is likely with standing vorticies just west of the mountains as outlined by Smith et al. (1997). These often take the form of two counter-rotating gyres connecting accelerated trade winds north-west and south-west of Puerto Rico with an in-folding sea-breeze zone over Mayaguez (cf. Fig. 10) that contribute to shallow afternoon thunderstorms. The direction of flow is critical: easterly winds provide a fetch >200 km, while other directions have a diminished over-island fetch.

From San Juan sounding data on the two case days, the lapse rate in the 0–2 km layer was $\approx -6°$C km^{-1} and 925-hPa zonal winds were 8.6–9.3 m s^{-1}. The Froude number as defined earlier is 1.07–1.10, so a short downstream wake is generated that meanders and traps vorticies over the western plains of Puerto Rico (Bennet et al. 1998). During summer season the trade winds flow across Cerro Punta, creating a convergent daytime circulation and lee-side convection, as schematically represented in Fig. 12a. In spring and autumn, periods of light winds bring a chance of blocking, but most of the rain then is synoptically forced by transient westerly troughs and tropical cyclones.

Surface heat fluxes estimated by the WRF model exceed 300 W m^{-2} over Puerto Rico during midday. Observations tend to support this value: (cf. Table 3). Air temperatures of 32°C, winds of 3–9 m s^{-1} and soil water fraction $\approx 40\%$ were found. Specific humidity increased from 15.3 to 17.9 g kg^{-1} on the coast and from 12.2 to 17.0 g kg^{-1} in the mountains from 0900 to 1400 LST, as solar radiation reached ≈ 800 W m^{-2}. These observations indicate that the uplift of humid air and evapotranspiration contributes to ABL moistening (cf. photo Fig. 12b). We can estimate the mean precipitation rate using the observations here and the relation: $P = \rho(W)(\partial qs/\partial t)\partial z(E)$, where P is precipitation rate, ρ is density, W is vertical motion forced by convergence, $\partial qs \approx 10^{-4}$ (change of specific humidity), $\partial t \approx 1$ h, a typical lifespan of a thunderstorm (3.6×10^3 s), ∂z is the depth of the thunderstorm updraft, and $E \approx 10^{-1}$ is the local cloud precipitation efficiency (cf. Fig. 2c). Other input values: $\rho \approx 1.15$ kg m^{-3}, $\partial z \approx 5 \times 10^3$ m (refer Fig. 7 or 11), $\partial qs \approx 0.1$ g kg^{-1} (from the Mayaguez dew point) and $W_{850-400\,hPa} \approx 10^{-1}$ m s^{-1} (WRF analysis at 1400 LST). We find a precipitation rate $P = 1.6 \times 10^{-8}$ m s^{-1} or 5.7 mm h^{-1}. This value is consistent with the mean daily observed rainfall in summer over western Puerto Rico.

5 Conclusions

The mean boundary-layer development over Puerto Rico was studied using the existing network of observations, radiosonde profiles, satellite and radar images, and NARR and WRF
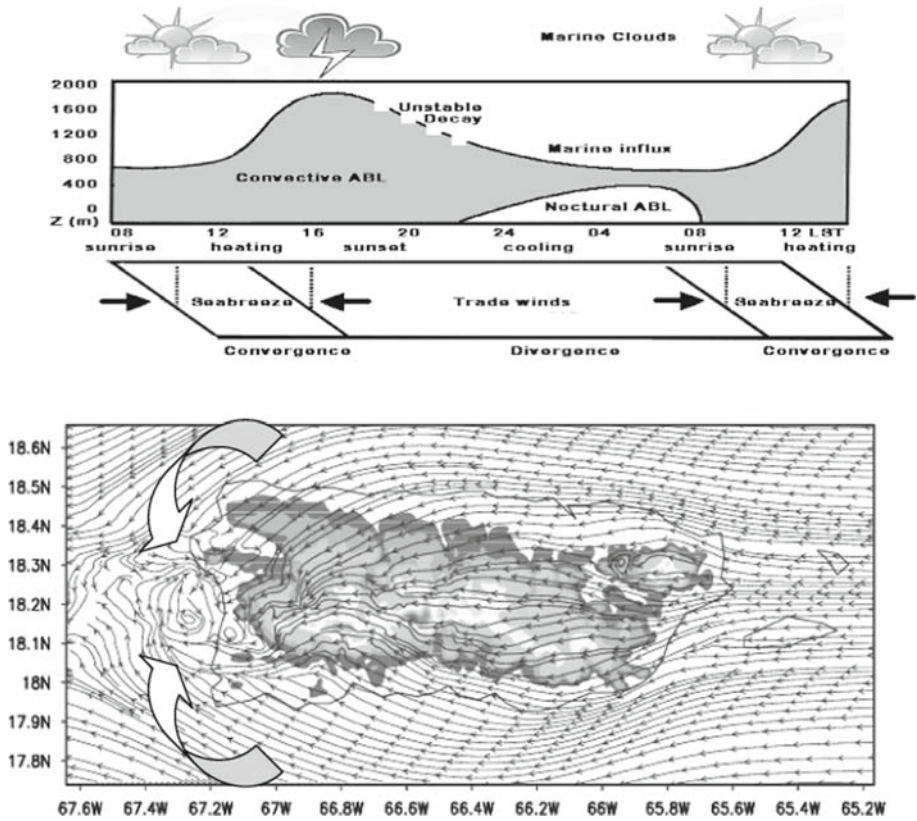
Fig. 12 **a** Schematic illustration of Puerto Rican ABL evolution over the diurnal cycle (adapted from Schafer et al. (2001)); **b** idealized simulation at 1400 LST with 10-m AGL wind streamlines illustrating bow-wave, mountain wake, leeward eddies, and counter-rotating gyres (orography shaded from 100 to 1,000 m). The simulation is after 12 h of integration with a moist adiabatic lapse rate, ABL easterly wind of 5 m s^{-1} and diurnal heating

model-assimilated fields. No field data were specifically collected, yet it was possible to describe the diurnal cycle and its mesoscale features during undisturbed weather conditions:

1. Following sunrise, surface heating creates a thermal low and convective boundary layer over western Puerto Rico which draws trade winds from the north and south coasts. An onshore low-level flow of ≈ 4 m s^{-1} develops along the west coast and intersects a turbulent wake cast by the central mountains.

2. By midday convergence lines develop in the vicinity of Mayaguez. The summer air mass is moist and unstable and shallow afternoon thunderstorms drift westward. Air temperatures reach 33°C, dew points 24°C, and CAPE values exceed 1500 J kg^{-1} on days when localized convection brings rainfall of ≈ 10 mm h^{-1}.

3. By late afternoon thunderstorms have collapsed, cooling the surface and allowing trade winds to resume. During the night, radiatively cooled air drains from the mountain and joins the trade winds to 'reset the diurnal clock' for the next day. The diurnal cycle is schematically represented in Fig. 12a.

This study has described variations of the ABL across Puerto Rico based on mesoscale reanalysis and model simulations. Existing in-situ data in 2006 were limited to hourly surface observations mainly around the coast and radiosonde profiles upwind. Thus we were unable to verify many aspects of NARR and operational WRF products. Nonetheless, much was learned about the ABL over Puerto Rico from conventional sources. The 1-km resolution WRF model simulations for two of the cloud band cases provided further insight to the processes setting up the afternoon convection near Mayaguez.

The ability of the model to describe wind confluence, ABL response to surface heating and short-lived thunderstorms was evaluated with a view to improved short-range weather forecasting. The WRF model replicated the moist unstable profile of mid-summer in Puerto Rico, but CAPE values were 30% underpredicted at 12-h lead time. The model simulated the development of short-lived thunderstorms over the west coast, and the underlying wind confluence and moisture loading. Surface observations showed that winds along the south-western coast rotate ≈90 degrees to the right during midday as dewpoint temperatures increase from 21 to 24°C. The simulated convection flared between 1400 and 1600 LST in agreement with satellite and radar images. The model-predicted cloud-top temperatures reached −40°C from 1500 to 1600 LST near Mayaguez, but scarce observations suggest shallower convection. The west coast sea breeze was simulated to interact with the mountain wake shed by the central ridge. This complexity is represented in the model, but verification data are limited over western Puerto Rico. Future studies will benefit from new sources of data including the Lajas wind profiler and an expanding network of automatic weather stations.

Further idealized WRF experiments (cf. Fig. 12b) involving incremental changes of low-level wind direction, surface heating, and the subsidence inversion, would help distinguish kinematic and thermodynamic effects. There is verification data on heat fluxes and horizontal winds that could be used in model 'calibration', but data on the vertical structure of circulations and ABL depth are limited. Aerial surveys could be done to provide this sort of information, in conjunction with weather radar analyses. If a field campaign were to be conducted, in addition to aircraft reconnaissance and the placement of covariance flux towers, the installation of a wind profiling radar in Mayaguez would aid our understanding. Then model sensitivity studies would better discriminate the influences of the sea breeze, orography and evapotranspiration (Weckwerth et al. 2004; Jankov et al. 2005).

References

Allen RG, Walter IA, Elliott R, Howell R, Itenfisu D, Jensen M, Snyder RL (2005) The ASCE standardized reference evapotranspiration equation. Environmental and Water Resources Inst., American Society Civil Engineers, 57 pp

Amador JA (1998) A climatic feature of the tropical Americas: the trade wind easterly jet. Top Meteorol Oceanogr 5(2):1–13

Baik JJ (1992) Response of a stably stratified atmosphere to low-level heating: an application to the heat island problem. J Appl Meteorol 31:291–303. doi:10.1175/1520-0450(1992)031<0291:ROASSA>2.0.CO;2

Bao JW, Michelson SA, Persson POG, Djalalova IV, Wilczak JM (2008) Observed and WRF-simulated low-level winds in a high-ozone episode during the Central California Ozone Study. J Appl Meteorol Climatol 47:2372–2394

Bennet S, Grusbisic V, Rasmussen RM (1998) Gravity waves, rainbands, and deep convection induced by trade wind flow over Puerto Rico. In: Proceedings of 12th conference on numerical weather prediction. AMS, Phoenix

Blanchard DO, López RE (1985) Spatial patterns of convection in south Florida. Mon Weather Rev 113:1282–1299. doi:10.1175/1520-0493(1985)113<1282:SPOCIS>2.0.CO;2

Bretherton CS, Smith C, Wallace JM (1992) An intercomparison of methods for finding coupled patterns in climate data. J Clim 5:541–560. doi:10.1175/1520-0442(1992)005<0541:AIOMFF>2.0.CO;2

Burk SD, Haack T, Rogers LT, Wagner LJ (2002) Island wake dynamics and wake influence on the evaporation duct and radar propagation. J Appl Meteorol 42:349–367. doi:10.1175/1520-0450(2003)042<0349:IWDAWI>2.0.CO;2

Carbone RE, Wilson JW, Keenan TD, Hacker JM (2000) Tropical island convection in the absence of significant topography. Part I: life cycle of diurnally forced convection. Mon Weather Rev 128:3459–3480. doi:10.1175/1520-0493(2000)128<3459:TICITA>2.0.CO;2

Carter MM, Elsner JB (1997) A statistical method for forecasting rainfall over Puerto Rico. Weather Forecast 12:515–525. doi:10.1175/1520-0434(1997)012<0515:ASMFFR>2.0.CO;2

Chang P, Saravanan R (2001) A hybrid coupled model study of tropical Atlantic variability. J Clim 14:361–390. doi:10.1175/1520-0442(2001)013<0361:AHCMSO>2.0.CO;2

Chen AA, Taylor M (2002) Investigating the link between early season Caribbean rainfall and the El Niño+1 year. Int J Climatol 22:87–106. doi:10.1002/joc.711

Chiao S (2006) Performance of planetary boundary layer schemes in the WRF model. In: Proceedings of 25th Army Science conference, Boulder, CO

Chopra KP (1973) Atmospheric and oceanic flow problems introduced by islands. Advances in Geophysics, vol 16, Academic Press, New York, USA, pp 298–416

Colle BA, Yuter SE (2006) The impact of coastal boundaries and small hills on the precipitation distribution across southern Connecticut and Long Island, New York. J Appl Meteorol 135:933–954

Cooper H, Garstang M, Simpson J (1982) The diurnal interaction between convection and peninsular-scale forcing over south Florida. Mon Weather Rev 110:486–503. doi:10.1175/1520-0493(1982)110<0486:TDIBCA>2.0.CO;2

Cuxart J, Jiménez MA, Martínez D (2006) Nocturnal meso-beta basin and katabatic flows on a midlatitude island. J Appl Meteorol 135:918–932

De Haan LL, Kanamitsu M, Lu CH, Roads JO (2007) A comparison of the Noah and OSU land surface models in the ECPC seasonal forecast model. J Hydrometeorol 8:1031–1048. doi:10.1175/JHM629.1

Enfield DB, Alfaro EJ (1999) The dependence of Caribbean rainfall on the interaction of the tropical Atlantic and Pacific Oceans. J Clim 12:2093–2103. doi:10.1175/1520-0442(1999)012<2093:TDOCRO>2.0.CO;2

Ek MB, Mitchell KE, Lin Y, Rogers E, Grunmann P, Koren V, Gayno G, Tarpley JD (2003) Implementation of Noah land surface model advances in the National Centers for Environmental Prediction operational mesoscale ETA model. J Geophys Res 108(D22):8851. doi:10.1029/2002JD003296

Etling D (1989) On atmospheric vortex streets in the wake of large islands. Meteorol Atmos Phys 41:157–164. doi:10.1007/BF01043134

Giannini A, Kushnir Y, Cane MA (2000) Interannual variability of Caribbean rainfall, ENSO, and the Atlantic Ocean. J Clim 13:297–311. doi:10.1175/1520-0442(2000)013<0297:IVOCRE>2.0.CO;2

Grubisic V, Smith RB, Schar C (1995) The effect of bottom friction on shallow-water flow past an isolated obstacle. J Atmos Sci 52:1985–2005. doi:10.1175/1520-0469(1995)052<1985:TEOBFO>2.0.CO;2

Hafner J, Xie SP (2003) Far-field simulation of the Hawaiian wake: sea surface temperature and orographic effects. J Atmos Sci 60:3021—3032

Hong S-Y, Dudhia J (2003) Testing of a non-local boundary layer vertical diffusion scheme in numerical weather prediction applications. In: Proceedings of 20th conference on weather analysis forecasting. AMS, Seattle, WA

Jankov I, Gallus WA, Segal M, Shaw B, Koch SE (2005) The impact of different WRF model physical parametreizations and their interactions on warm season MCS rainfall. Weather Forecast 20:1048–1060. doi:10.1175/WAF888.1

Jiang Q, Doyle JD (2008) On the diurnal variation of mountain waves. J Atmos Sci 65:1360–1377

Joyce RJ, Janowiak JE, Arkin PA, Xie P (2004) CMORPH: a method that produces global precipitation estimates from passive microwave and infrared data at high spatial and temporal resolution. J Hydrometeorol 5:487–503. doi:10.1175/1525-7541(2004)005<0487:CAMTPG>2.0.CO;2

Jury MR (2009) An inter-comparison of observational, reanalysis, satellite, and coupled model data on mean rainfall in the Caribbean. J Hydrometeorol 10:413–430

Jury MR, Malmgren BA, Winter A (2007) Sub-regional precipitation climate of the Caribbean and relationships with ENSO and NAO. J Geophys Res 112:D16107. doi:10.1029/2006JD007541

Keenan TD et al (2000) The Maritime Continent Thunderstorm experiment: overview and results. Bull Am Meteorol Soc 81:2433–2455. doi:10.1175/1520-0477(2000)081<2433:TMCTEM>2.3.CO;2

Kingsmill DE (1995) Convection initiation associated with a sea-breeze front, a gust front and their interaction. Mon Weather Rev 123:2913–2933. doi:10.1175/1520-0493(1995)123<2913:CIAWAS>2.0.CO;2

Liu C, Moncrieff MW (1996) A numerical study of the effects of ambient flow and shear on density currents. Mon Weather Rev 124:2282–2303. doi:10.1175/1520-0493(1996)124<2282:ANSOTE>2.0.CO;2

Malkus JS (1954) Some results of a trade cumulus cloud investigation. J Meteorol 11:220–237

Malkus JS (1955) The effects of a large island upon the trade-wind air stream. Q J Roy Meteorol Soc 81(350):538–550. doi:10.1002/qj.49708135003

May PT, Wilczak JM (1993) Diurnal and seasonal variations of boundary layer structure observed by a radar wind profiler and RASS. Mon Weather Rev 121:673–682. doi:10.1175/1520-0493(1993)121<0673:DASVOB>2.0.CO;2

Mesinger F et al (2006) North American regional reanalysis. Bull Am Meteorol Soc 87:343–360. doi:10.1175/BAMS-87-3-343

Mitchell KE et al (2002) The community Noah land surface model (LSM)-User's guide. In: Proceedings of 15th AMS conference on hydrology. American Meteorological Society, pp 180–183

Mlawer EJ, Taubman SJ, Brown PD, Iacono MJ, Clough SA (1997) Radiative transfer for inhomogeneous atmosphere: RRTM, a validated correlated-k model for the long-wave. J Geophys Res 102(D14):16663–16682. doi:10.1029/97JD00237

Muñoz E, Busalacchi AJ, Nigam S, Ruiz-Barradas A (2008) Winter and summer structure of the Caribbean low-level jet. J Clim 21:1260–1276. doi:10.1175/2007JCLI1855.1

Pagowski M, Hacker J, Bao JW (2005) Behaviour of WRF PBL schemes and land-surface models in 1-D simulation during BAMEX. WRF Users Workshop, June 27–30, Boulder, CO

Pearce RP, Smith RC, Malkus JS (1956) The calculation of a sea-breeze circulation in terms of the differential heating across the coast line. Q J Roy Meteorol Soc 82(352):235–241. doi:10.1002/qj.49708235211

Rasmussen RM, Smolarkiewicz PK, Warner J (1989) On the dynamics of Hawaiian cloud bands: comparison of model results with observations and island climatology. J Atmos Sci 46:1589–1608. doi:10.1175/1520-0469(1989)046<1589:OTDOHC>2.0.CO;2

Rogers E, Ek M, Lin Y, Mitchell K, Parrish D, DiMego G (2001) Changes to the NCEP Meso ETA analysis and forecast system: Assimilation of observed precipitation, upgrades in land-surface physics, modified 3-DVAR analysis. http://www.emc.ncep.noaa.gov/mmb/mmbpll/spring2001/tpb/

Schafer R, May PT, Keenan TD, McGuffie K, Ecklund WL, Johnston PE, Gage KS (2001) Boundary layer development over a tropical island during the Maritime Continent Thunderstorm Experiment. J Atmos Sci 58:2163–2179. doi:10.1175/1520-0469(2001)058<2163:BLDOAT>2.0.CO;2

Schar C, Smith RB (1993a) Shallow-water flow past isolated topography. Part I: vorticity production and wake formation. J Atmos Sci 50:1373–1400. doi:10.1175/1520-0469(1993)050<1373:SWFPIT>2.0.CO;2

Schar C, Smith RB (1993b) Shallow-water flow past isolated topography. Part II: transition to vortex shedding. J Atmos Sci 50:1401–1412. doi:10.1175/1520-0469(1993)050<1401:SWFPIT>2.0.CO;2

Smith RB, Grubisic V (1993) Aerial observations of Hawaii's wake. J Atmos Sci 50:3728–3750. doi:10.1175/1520-0469(1993)050<3728:AOOHW>2.0.CO;2

Smith RB, Gleason AC, Gluhosky PA, Grubišić V (1997) The wake of St. Vincent. J Atmos Sci 54:606–623. doi:10.1175/1520-0469(1997)054<0606:TWOSV>2.0.CO;2

Smolarkiewicz PK, Rasmussen RM, Clark TL (1988) On the dynamics of Hawaiian cloud bands: island forcing. J Atmos Sci 45:1872–1905. doi:10.1175/1520-0469(1988)045<1872:OTDOHC>2.0.CO;2

Szumowski MJ, Rauber RM, Ochs HT, Miller LJ (1997) The microphysical structure and evolution of Hawaiian rainband clouds. Part I: radar observations of rainbands containing high reflectivity cores. J Atmos Sci 54:369–385. doi:10.1175/1520-0469(1997)054<0369:TMSAEO>2.0.CO;2

Wakimoto RM, Atkins NT (1994) Observations of the sea-breeze front during CaPE. Part I: single-Doppler, satellite, and cloud photogrammetry analysis. Mon Weather Rev 122:1092–1114. doi:10.1175/1520-0493(1994)122<1092:OOTSBF>2.0.CO;2

Weckwerth TM et al (2004) An overview of the international H2O project (IHOP_2002) and some preliminary highlights. Bull Am Meteorol Soc 85:253–277. doi:10.1175/BAMS-85-2-253

Wilson JW, Schreiber WE (1986) Initiation of convective storms at radar-observed boundary-layer convergence lines. Mon Weather Rev 114:2516–2536. doi:10.1175/1520-0493(1986)114<2516:IOCSAR>2.0.CO;2